JOURNAL OF APPLIED PHYSICS **102**, 114108 (2007)

Piezoresponse force spectroscopy of ferroelectric-semiconductor materials

Anna N. Morozovska[a),b)] and Sergei V. Svechnikov
V. Lashkaryov Institute of Semiconductor Physics, National Academy of Science of Ukraine, 41, pr. Nauki, 03028 Kiev, Ukraine

Eugene A. Eliseev
Institute for Problems of Materials Science, National Academy of Science of Ukraine, 3, Krjijanovskogo, 03142 Kiev, Ukraine

Stephen Jesse, Brian J. Rodriguez, and Sergei V. Kalinin[c)]
Materials Sciences and Technology Division, Oak Ridge National Laboratory, Oak Ridge, Tennessee 37831, USA and the Center for Nanophase Materials Sciences, Oak Ridge National Laboratory, Oak Ridge, Tennessee 37831, USA

(Received 13 August 2007; accepted 5 October 2007; published online 10 December 2007)

Piezoresponse force spectroscopy (PFS) has emerged as a powerful technique for probing highly localized polarization switching in ferroelectric materials. The application of a dc bias to a scanning probe microscope tip in contact with a ferroelectric surface results in the nucleation and growth of a ferroelectric domain below the tip, detected though the change of local electromechanical response. Here, we analyze the signal formation mechanism in PFS by deriving the main parameters of domain nucleation in a semi-infinite ferroelectric semiconductor material. The effect of surface screening and finite Debye length on the switching behavior is established. We predict that critical domain sizes and activation barrier in piezoresponse force microscopy (PFM) is controlled by the screening mechanisms. The relationships between domain parameters and PFM signal is established using a linear Green's function theory. This analysis allows PFS to be extended to address phenomena such as domain nucleation in the vicinity of defects and local switching centers in ferroelectrics. © *2007 American Institute of Physics*. [DOI: 10.1063/1.2818370]

I. INTRODUCTION

In the last decade, ferroelectric materials have attracted much attention for electronic device applications such as nonvolatile memories,[1] ferroelectric data storage,[2,3] or as a platform for nanofabrication.[4] This has stimulated a number of theoretical and experimental studies of ferroelectric properties in low dimensional systems,[5,6] including the size limit for ferroelectricity[7–9] and intrinsic switching[10] in thin films, and unusual polarization ordering in ferroelectric nanoparticles and nanowires.[11,12] Further progress in these fields necessitates fundamental studies of ferroelectric domain structures and dynamics and polarization-switching phenomena on the nanoscale. In the last decade, the invention of piezoresponse force microscopy[13–17] (PFM) has enabled sub-10 nm resolution imaging of crystallographic and molecular orientations, surface termination, and domain structures in ferroelectric and piezoelectric materials. In materials with switchable polarization, the smallest domain size reported to date is 5 nm and local polarization patterning down to 8 nm has been demonstrated.[18] Finally, local electromechanical hysteresis loop measurements (piezoresponse force spectroscopy) have been developed,[16] providing insight into local switching behavior and mechanisms of polarization switching on the nanoscale.

The characteristic shapes of the electromechanical hysteresis loops in PFM and macroscopic polarization-electric (P-E) field loops are similar, resulting in a number of attempts to interpret PFM hysteresis loops in terms of macroscopic materials properties. However, in the macroscopic case, the loop shape is determined by statistical characteristics of collective processes in ferroelectric ceramics, single crystals, or thin films, including reversible and irreversible displacements of existing domain walls,[19] wall interactions with grain boundaries, defects, and strain fields, and nucleation of domains[20,21]

Conversely, in the PFM experiment, the electric field is highly localized in the vicinity of the atomic force microscope (AFM) tip, with the maximum value achieved at the tip-surface contact. Therefore, domain nucleation is initiated directly below the tip, with subsequent vertical and lateral domain growths. This scenario has been supported by numerous experimental and theoretical studies of local ferroelectric domain switching.[22–26] Thus, unlike macroscopic case, PFM experiment addresses switching on a single domain level. The PFM hysteresis loop shape is determined by the convolution of the signal generation volume and the shape of nascent domain. Despite the qualitative similarity between the hysteresis loop shape in macroscopic and microscopic cases, the fundamental mechanisms behind the loop formation are principally different, necessitating the quantitative analysis of local electromechanical hysteresis loop formation in PFM.

Here, we analyze the hysteresis loop formation mechanisms in PFM and develop the theoretical framework for the interpretation of the PFM hysteresis measurements. Recent achievements in PFM and models for the interpretation of

---

[a)] Authors to whom correspondence should be addressed.
[b)] Electronic mail: morozo@i.com.ua.
[c)] Electronic mail: sergei2@ornl.gov.

piezoresponse force spectroscopy (PFS) are summarized in Sec. II. Thermodynamics of domain switching, the role of surface screening, and finite material conductivity are analyzed in Sec. III. The relationship between geometric parameters of a domain and the PFM signal for ferroelectric and ferroelectric-semiconductor is derived in Sec. IV. The experimental results are briefly discussed in Sec. V, and the role of pinning on hysteresis loop formation is considered. We also demonstrate that PFM spectroscopy can provide information on the local mechanism for domain nucleation and the thermodynamic parameters of the switching process, and discuss the future potential of PFS to probe nanoscale ferroelectric phenomena.

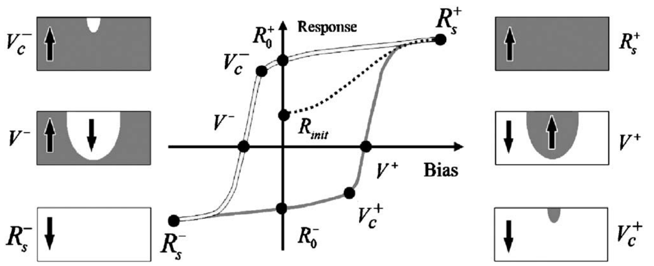

FIG. 1. (a) PFM hysteresis loop. Forward and reverse coercive voltages, V^+ and V^-, nucleation voltages, V_c^+ and V_c^-, and forward and reverse saturation and remanent responses, R_0^+, R_0^-, R_s^+, and R_s^-, are shown. The work of switching A_s is defined as the area within the loop. The domain structure at the characteristic points of the forward (right) and reverse (left) branches of the hysteresis loop is also shown. Arrows indicate the polarization direction.

II. CURRENT RESULTS ON NANOSCALE POLARIZATION DYNAMICS

A. Phenomenological studies of domain dynamics

PFM imaging and spectroscopy are based on the detection of bias-induced piezoelectric surface deformation.[27] The tip is brought into contact with the surface and the piezoelectric response of the surface is detected as the first harmonic component of bias-induced tip deflection. The amplitude of piezoresponse signal defines the local electromechanical activity of the surface, while the phase provides predominant domain orientation, from which polarization orientation maps (domain structure) can be reconstructed. Thus, PFM is ideally suited for determination of *static* polarization distributions on the ~10 nm length scales and above.

Two of the key questions in understanding ferroelectric materials are the mechanisms for polarization switching and the role of defects, vacancies, domain walls, etc., on switching processes, i.e., polarization *dynamics*. A closely related issue is the nature of the defect sites that allow domain nucleation at low electric fields (Landauer paradox).[28] Dynamic behavior of polarization can be addressed by switching experiments. The application of dc bias to the PFM tip can result in local polarization switching below the tip, thus enabling the creation of domains. Subsequent examination of domain structures produced by the switching event provides the information on switching mechanism. Recent studies by Gruverman *et al.* have shown that domain nucleation in ferroelectric capacitors is always initiated at the same defect regions;[29] similarly, the grain boundaries were shown to play an important role in domain wall pinning.[30] Paruch and coworkers have used local studies of domain growth kinetics[31] and domain wall morphology[32] to establish the origins of disorder in ferroelectric materials. Dawber *et al.* interpreted the nonuniform wall morphologies as evidence for skyrmion emission during domain wall motion.[33] Most recently, Agronin *et al.* have observed domain pinning on structural defects.[34]

The primary limitation of these studies of domain growth is the large time required to perform multiple switching and imaging steps. Moreover, the information is obtained on the domain growth initiated at a single point for different bias conditions, thus precluding systematic studies of microstructure influence on domain growth process. An alternative approach to study domain dynamics in the PFM experiment is based on local spectroscopic measurements, in which the domain switching and electromechanical detection are performed simultaneously, yielding a local electromechanical hysteresis loop. In-field hysteresis loop measurements were first reported by Birk *et al.*[35] using a scanning tunneling microscopy (STM) tip and Hidaka *et al.*[16] using an AFM tip. This approach was later used by several groups to probe crystallographic orientation and microstructure effects on switching behavior.[36–41] Recently, PFM spectroscopy has been extended to an imaging mode using an algorithm for fast (100–300 ms) hysteresis loop measurements developed by Jesse *et al.*[42]

The progress in experimental studies has stimulated a parallel development of theoretical models to relate PFM hysteresis loop parameters and materials properties. A number of such models are based on the interpretation of phenomenological characteristics of PFS hysteresis loops similar to macroscopic P-E loops, such as slope, imprint bias, coercive bias, remanent response, and work of switching,[43,44] as illustrated in Fig. 1. A number of authors attempted to relate local PFM hysteresis loops and macroscopic *P-E* measurements, often demonstrating good agreement between the two.[45–48] Several groups combined local detection by PFM with a uniform switching field imposed through the thin top electrode to study polarization switching in ferroelectric capacitor structures. Spatial variability in switching behavior was discovered by Gruverman *et al.* and attributed to strain[49] and flexoelectric[50] effects and defect regions.[29,51]

The rapidly growing number of experimental observations and recent developments in PFS requires understanding not only phenomenological but also quantitative parameters of hysteresis loops, such as numerical value of the coercive bias, the nucleation threshold, etc. Kalinin *et al.*[37] have extended the one-dimensional (1D) model by Ganpule *et al.*[52] to describe PFM loop shape in the thermodynamic limit. Wu *et al.* have postulated the existence of nucleation bias from PFM loop observations,[53] in agreement with theoretical studies by Abplanalp,[22] Kalinin *et al.*,[24] Emelyanov,[25] and Morozovska and Eliseev.[26] Finally, Jesse *et al.*[42] have analyzed hysteresis loop shape in kinetic and thermodynamic limits for domain formation. However, in all cases, the model was essentially 1D, ignoring the fundamental physics of domain formation. Here, we develop the full three-dimensional (3D) model for hysteresis loop formation in PFM including the

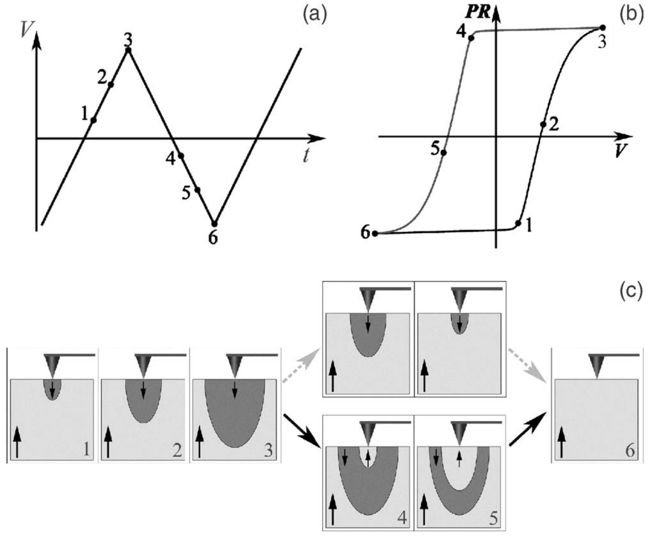

FIG. 2. Domain evolution with bias dependence for materials with different pinning strengths. (a) Time dependence of voltage and (b) schematics of hysteresis loop. (c) Schematics of the domain growth process. In the purely thermodynamic case (dashed arrows), the domain shrinks with decreased voltage [path 3−>2−>1 in (b)]. To account for a realistic loop, the domain size does not change on 3–4 and a domain of opposite polarity nucleates on paths 4–6. At point 6, antiparallel domain walls annihilate.

bias dependence of domain parameters and the relationship between the PFM signal and domain geometry for a general case of ferroelectric semiconductor for different screening conditions on the surface.

B. Theory of domain switching in PFM

The analysis of the tip-induced domain growth process during hysteresis loop measurements in PFS should describe the individual stages in Fig. 2, including domain nucleation and growth for forward bias sweep, with either reverse domain nucleation or shrinkage on reverse bias sweep. A number of phenomenological models have been developed based on the classical work of Landauer,[28] where domain nucleation in ferroelectrics-dielectrics under a *homogeneous* electric field was studied. In the original work by Abplanalp,[22] polarization reversal in the *inhomogeneous* electric field of an AFM tip for a semiellipsoidal domain with infinitely thin domain walls under the absence of bound charges compensation is considered. The tip was modeled using a point-charge system. It was also predicted that due to the finite charge-surface separation, domain nucleation requires nonzero nucleation bias. This voltage threshold for domain nucleation in the *inhomogeneous* electric field of an AFM tip was then studied by Molotskii,[54] Kalinin *et al.*,[24] Emelyanov,[25] and Morozovska and Eliseev[26] using a variety of tip models, as described below.

Using Landauer model and a point-charge approximation for the electric field of an AFM tip, Molotskii[23] obtained elegant closed-form analytical expressions for the domain size dependence on the applied voltage in the case when the surface charges were completely compensated by the external screening ones. Kalinin *et al.*[24] considered the domain nucleation allowing for the electromechanical coupling inside a ferroelectric medium using both the sphere-plane model of the AFM tip and a rigorous solution for the tip-surface indentation problem. It was shown numerically and analytically that the domain nucleation is possible above the threshold value of voltage applied to the tip, i.e., a potential barrier for nucleation exists. Depending on the activation energy, the domain nucleation was classified in terms of first and second order phase transitions. Similar results were later obtained by Emelyanov,[25] who considered the nucleation of semiellipsoidal domains by voltage modulated AFM in ferroelectric films within the framework of classical thermodynamic approach. He analyzed the switching in thin films and classified stages of the switching process and proved that semiellipsoidal domains are unstable and transform into cylindrical domains spanning the thickness of the film when reach the bottom electrode.

Recently Morozovska and Eliseev[26] have developed the thermodynamic theory of nanodomain tailoring in thin ferroelectrics films allowing for semiconducting properties, screening, and size effects. The analytical results proved that the nucleation of a cylindrical domain intergrown through the thin film is similar to the first order phase transition. However, the screening effect on the semiellipsoidal domain formation in thicker films, ferroelectric hysteresis and piezoelectric response were not considered.

Following our recent papers,[55,56] here we extend the thermodynamic theory for hysteresis loop formation in PFM, and analyze the effects of surface screening and finite conductivity of the material. These results are compared to experimental studies, elucidating role of kinetic effects and pinning on domain formation.

III. PHENOMENOLOGICAL DESCRIPTION OF NANOSCALE POLARIZATION REVERSAL

A. Ambient conditions and screening mechanisms

Theoretical description of domain formation with local probe under ambient conditions should take into consideration the layer of adsorbed water (meniscus) located below the tip apex,[26,54] and, more generally, the dynamic and static surface charging and screening phenomena.[57–59] In recent studies, the role of these charges on polarization dynamics in PFM has been illustrated.[60–62] Hence, here we assume for generality that region between the tip apex and domain surface has effective dielectric permittivity, ε_e. The polarization reversal on the domain face may be accompanied by several mechanisms of surface recharging up to value σ_S, different from the initial charge $\sigma_S^0 = -P_S$, including the following.

(a) Screening by ambient charges on the free surface. This process is relatively slow (∼10 min) and is limited by the kinetics of the mass exchange in the vicinity of the sample.[58,59]

(b) Surface charging/electrochemical reactions in the adsorbed water layer at high voltages. The presence of this surface charge on an oxide surface in ambient is a well-known phenomenon, as confirmed by charge retention and diffusion on nominally conductive surfaces upon contact electrification or under lateral biasing.[63–65]

(c) In the absence of tip-surface charge transfer, the tip-induced field effect in materials with finite conductivity can result in surface recharging up to value $\sigma_S \neq \sigma_S^0$. This mechanism is active when either the tip is covered by an oxide or tip-surface dielectric gap exists and direct tip-surface charge transfer is impossible.

Complementary to surface screening is the screening of the domain wall in the bulk.[66] The screening charge is concentrated in a thin layer around the semiellipsoidal domain apex allowing for bend bending and strong field effects in the vicinity of oppositely charged domain wall. Captured charges, σ_b, screen the spontaneous polarization, $+P_S$, and thus partially compensate the strong depolarization field in the system. The screening effect of the moving domain wall is corroborated by numerous experimental facts proving that neighboring domains in dense array do not interact significantly during their formation, reorientation, and storage.[67] Depending on the domain shape, $\sigma_b(z)$ distribution is different for an oblate or spikelike domain apex.

Here we assume that the average surface charge density on the surface, $\Delta\sigma_S = \sigma_S - \sigma_S^0$ has the form

$$\Delta\sigma_S = \begin{cases} \sigma_S + P_S, & \sqrt{x^2+y^2} < r \\ 0, & \sqrt{x^2+y^2} > r, \end{cases} \tag{1}$$

i.e., screening is dominated by polarization switching. In the general case, $-P_S \leqslant \sigma_S \leqslant P_S$. When the charge compensation mechanism on the surface and around the domain wall moving in the bulk are the same, screening charge distribution $\sigma_b(z)|_\Sigma$ on the domain sidewall Σ is equal to $-(P_S + \sigma_S)n_z(z)$, where n_z is z-component of the domain outer normal, $\mathbf{n}$, allowing for the initial screening charge $\sigma_S^0 = -P_S$ conservation. In general case they are different, from completely unscreened (e.g., rigid dielectric) to the full screening, i.e., $-2P_S n_z(z) \leqslant \sigma_b(z)|_\Sigma \leqslant 0$ (ferroelectric-semiconductor with small Debye length).

The relevance of the specific screening mechanism on polarization-switching dynamics depends on the relationship between the corresponding relaxation time, τ_S, and voltage pulse time, τ_U (i.e., recording time of the domain). "Fast" screening mechanisms with $\tau_S \leqslant \tau_U$ significantly affect the switching process, whereas the "slow" ones with $\tau_S \gg \tau_U$ can be ignored. However, these slow mechanisms can significantly affect the domain stability after switching by providing additional channels for minimizing depolarization energy.

B. The problem statement

In the ferroelectrics-semiconductor bulk within the linear approximation the charge density $\rho_f(\mathbf{r})$ satisfies the equation $\rho_f(\mathbf{r}) \approx -\varepsilon_0\kappa\varphi(\mathbf{r})/R_d^2$,[66] where R_d is Debye screening radius and $\kappa = \sqrt{\varepsilon_{11}\varepsilon_{33}}$ is the effective dielectric constant.[68] The potential distribution $\varphi(\mathbf{r})$ is determined by the Poisson equation with the following boundary conditions for potential and normal displacement components, $D_{n\text{ext}} - D_{n\text{int}} = \sigma_b(z)$ on the domain sidewall Σ, and $D_{n\text{ext}} - D_{n\text{int}} = \sigma_S$ on the sample surface $z=0$:

$$\begin{gathered} \Delta\varphi_0(\mathbf{r}) = 0, \quad z \leqslant 0, \\ \varphi_0|_{\mathbf{r}\in\text{tip}} = U, \quad \varphi_0(z=0) = \varphi(z=0), \\ \varepsilon_0\left(\varepsilon_e\frac{\partial\varphi_0}{\partial z} - \varepsilon_{33}\frac{\partial\varphi}{\partial z}\right)\bigg|_{z=0} = \begin{cases} \sigma_S - P_S, & \sqrt{x^2+y^2} < r \\ 0, & \sqrt{x^2+y^2} > r, \end{cases} \\ \left(\varepsilon_{33}\frac{\partial^2}{\partial z^2} + \varepsilon_{11}\Delta_\perp\right)\varphi(\mathbf{r}) - \frac{\varphi(\mathbf{r})}{R_d^2} = 0, \quad z \geqslant 0, \\ \varepsilon_{33}\varepsilon_0\left(\frac{\partial\varphi_{\text{int}}}{\partial\mathbf{n}} - \frac{\partial\varphi_{\text{ext}}}{\partial\mathbf{n}}\right)\bigg|_\Sigma = 2P_S n_z + \sigma_b|_\Sigma, \quad \varphi(z=h) = 0. \end{gathered} \tag{2}$$

The electric field induced by the PFM probe, $\mathbf{E} = -\nabla\varphi(\mathbf{r})$, is calculated using an appropriate model for the probe tip. For domain nucleation and initial growth stages we use the local point charge model[69] that adequately describes the probe electric field in the immediate vicinity of the tip-surface junction. For the later growth stages one could use a more rigorous but complex sphere-plane model, when the conductive probe apex is considered as a metallic sphere of radius R_0 under the voltage U. Results obtained for capacitance approximation (point charge at distance R_0 from the surface) were analyzed for comparison. When the electrostatic potential $\varphi(\mathbf{r})$ is determined, the next step is to determine the electrostatic energy $\Delta\Phi_{\text{el}} = \Delta\int dv(\mathbf{D}\cdot\mathbf{E} - \mathbf{P}_S\cdot\mathbf{E})/2\varepsilon_0$ and wall energy $\Phi_S(r,l)$ of the domain, as described below.

C. Effect of screening on free-energy functional

To determine the thermodynamic parameters of the switching process including the nucleation bias and equilibrium domain geometry, the domain size is calculated for semi-infinite ferroelectric material using the thermodynamic formalism developed by Morozovska and Eliseev.[70] The free energy of the semiellipsoidal domain with radius, r, and length, l, formed below the tip under the action of bias, U, is

$$\Phi(U,r,l) = \Phi_U(U,r,l) + \Phi_S(r,l) + \Phi_D(r,l). \tag{3}$$

Typically $\Phi_U(r,l)$ has been considered as the domain polarization interaction energy with tip-induced electric field. However, the analysis of domain energy necessitates the consideration of the contribution of the surface energy term, $\Delta\Phi_\sigma \sim \int ds\Delta\sigma_S\varphi(\mathbf{r})$, into $\Phi_U(r,l)$, which depends on the mechanism of the screening process. Here, two limiting cases of (i) perfect and (ii) imperfect tip-surface electric contacts are distinguished.

(i) When the transfer of external free charges can cause the redistribution of $\Delta\sigma_S$, the term $\Delta\Phi_\sigma = 0$. For instance, free screening charges σ_S may be located inside the plain conducting electrode (Landauer model) or flattened tip apex that is in direct electric contact with the sample surface [Fig. 3(a)].

(ii) The charges σ_S are captured by the sample surface and separated from the charged tip by the (ultra)thin dielectric gap excluding direct tip-surface charge transfer. For the case the term $\Delta\Phi_\sigma \sim \int\Delta\sigma_S\varphi(\mathbf{r})$ along

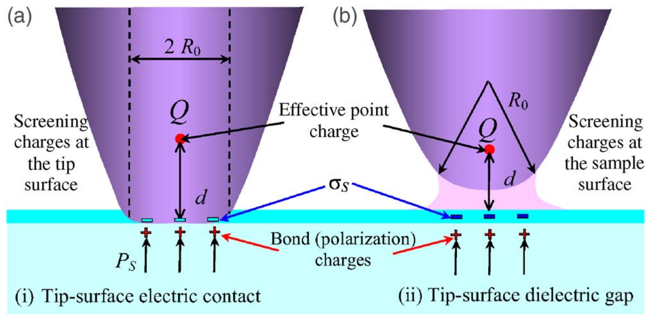

FIG. 3. (Color online) (a) Free screening charges σ_S located at the surface of flattened tip apex that is in direct electric contact with the sample surface. (b) Screening charges σ_S captured by the sample surface and separated from the charged tip by the dielectric gap.

with the conventional one $\Delta\Phi_P \sim -2\int P_S\varphi(\mathbf{r})$ should be included into the electrostatic interaction energy [Fig. 3(b)].

For these two limiting cases (i) and (ii) we derive Pade approximation for the interaction energy

$$\Phi_U(r,l) \approx \frac{R_d U C_t/\varepsilon_0}{(\kappa+\varepsilon_e)R_d + 2\kappa\sqrt{d^2+r^2}}\left[\frac{(\Delta\sigma_S - 2P_S)r^2}{\sqrt{r^2+d^2}+d} + \frac{(\sigma_b+2P_S)r^2}{\sqrt{r^2+d^2}+d+(l/\gamma)}\right]. \tag{4}$$

Hereinafter $\Delta\sigma_S=0$ for case (i) and $\Delta\sigma_S=\sigma_S+P_S$ for case (ii). The effective value of σ_b is within the range $-2P_S \leqslant \sigma_b \leqslant 0$. Distance d is the effective charge-surface separation, describing the probe tip electric field (typically $d = 1-100$ nm). The distance d is proportional to the tip curvature, R_0, and tip apex-sample separation, ΔR, which is typically nonzero for case (ii). ε_e and $\kappa=\sqrt{\varepsilon_{33}\varepsilon_{11}}$ are the ambient and ferroelectric dielectric permittivities, C_t is the probe tip effective capacity, and $\gamma=\sqrt{\varepsilon_{33}/\varepsilon_{11}}$ is dielectric anisotropy. Under the conditions $R_0 \gg \Delta R$ and $R_d \gg R_0$ the distance $d=\varepsilon_e R_0/\kappa$ and capacity $C_t \approx 2\pi\varepsilon_0(\varepsilon_e+\kappa)d$ within the framework of local point-charge model.[55,69] Within the framework of total point-charge model for a spherical tip apex of radius R_0 that touches the surface, $C_t \approx 4\pi\varepsilon_0\varepsilon_e R_0[(\kappa+\varepsilon_e)/(\kappa-\varepsilon_e)]\ln[(\varepsilon_e+\kappa)/2\varepsilon_e]$, $d \approx 2\varepsilon_e R_0 \ln[(\varepsilon_e+\kappa)/2\varepsilon_e]/(\kappa-\varepsilon_e)$. Within the framework of capacitance approximation $d=R_0+\Delta R \approx R_0$ and C_t is the same as for total point-charge model.

The domain wall surface energy, $\Phi_S(r,l)$, is

$$\Phi_S(r,l) = \pi\psi_S l r\left(\frac{r}{l} + \frac{\arcsin\sqrt{1-r^2/l^2}}{\sqrt{1-r^2/l^2}}\right) \approx \frac{\pi^2\psi_S l r}{2}\left[1 + \frac{2(r/l)^2}{4+\pi(r/l)}\right]. \tag{5}$$

Here we assume that the domain wall thickness is negligibly small in comparison with domain sizes and the domain wall surface energy, ψ_S, is constantly independent of the wall orientation. In accordance with recent data, the thickness of domain wall is of the order of several lattice constants in perovskite ferroelectrics. However, the value ψ_S discrepancy encountered in literature is very high, e.g., $1-10\ \mathrm{mJ/m^2}$ for $BaTiO_3$ (Ref. 71) and $40-400\ \mathrm{mJ/m^2}$ for $LiTaO_3$.[72–74] Hereinafter we consider ψ_S as a fitting parameter.

It has been previously shown[55] that depolarization field energy is created by the bulk[75] (Landauer contribution) and the surface charges. For the considered case of tip-induced nucleation, upper estimation of depolarization field energy $\Phi_D(r,l)$, is

$$\begin{aligned}\Phi_D(r,l) &\leqslant \left(\frac{4\pi r^3 R_d l[(P_S-\sigma_S)^2 - 2(\sigma_b+2P_S)(P_S-\sigma_S)\mathrm{Int}(l/\gamma r)]}{\varepsilon_0\{l[3\pi R_d(\kappa+\varepsilon_e)+16\kappa r]+8\gamma\kappa R_d r\}}\right.\\ &\quad + \frac{4\pi r^3 R_d l(\sigma_b+2P_S)^2}{\varepsilon_0\kappa[l(6\pi R_d+16r)+8\gamma R_d r]}\\ &\quad \left.\times\left[1+\frac{\kappa-\varepsilon_e}{\kappa+\varepsilon_e}\mathrm{Int}(2l/\gamma r)\right]\right),\end{aligned} \tag{6}$$

where $\mathrm{Int}(\lambda)=\int_0^\infty 3\pi/4[\mathrm{J}_1(x)/x]^2\exp(-\lambda x)dx$. Using typical condition $R_d \gg r$ (large Debye length), we obtained the following Pade approximation for depolarization field energy:

$$\Phi_D(r,l) \approx \frac{\pi(P_S-\sigma_S)^2}{2\varepsilon_0\kappa\gamma}r^2 l \text{ at } l \ll \gamma r \quad \text{while } \Phi_D(r,l) \approx \frac{4(P_S-\sigma_S)^2}{3\varepsilon_0(\kappa+\varepsilon_e)}r^3 \text{ at } l \gg \gamma r.$$

D. Thermodynamics of polarization switching

The thermodynamics of the switching process can be analyzed from the bias dependence of free energy, Eq. (3). The dependence of $\Phi(r,l)$ on domain radius r, and length l, can be represented as a free-energy surface for each value of U. For small biases, $U<U_S$, the free energy is a positively defined monotonic function of domain sizes, corresponding to the absence of a stable switched domain. At $U=U_S$ the saddle point appears. For biases $U_S<U<U_{\mathrm{cr}}$, the local minimum $\Phi_{\min}>0$ arises, corresponding to a metastable domain of sizes l and r. For $U=U_{\mathrm{cr}}$, the absolute minimum $\Phi_{\min}=0$ is achieved corresponding to a thermodynamically stable domain of sizes l_{cr} and r_{cr}. These correspond to minimal stable domain size that can be created by PFM. Finally, for $U \geqslant U_{\mathrm{cr}}$, the stable domain of sizes l and r forms.

The metastable or stable minimum point and the coordinate origin are separated by the saddle point $\{r_S,l_S\}$. The corresponding energy $\Phi(r_S,l_S)=E_a$ is the activation barrier for domain nucleation, while domain parameters $\{r_S,l_S\}$ represent the critical nucleus size. This behavior is due to the finite value of electric field on the surface, precluding nucleation in the zero-bias limit.

The evolution of the free-energy surface with bias, i.e., the thermodynamics and kinetics of switching process, is strongly affected by surface and bulk screening. The free-energy maps at voltages $U=U_{\mathrm{cr}}$ are shown in Fig. 4 for different screening conditions. Cases (i) and (ii) coincide for $\sigma_S=-P_S$ and $\sigma_b=0$ as expected, so Fig. 4(a) is common for all cases. The scenario in which the screening charges redistribution energy $\Delta\Phi_\sigma \sim \Delta\sigma_S$ is included into the free energy

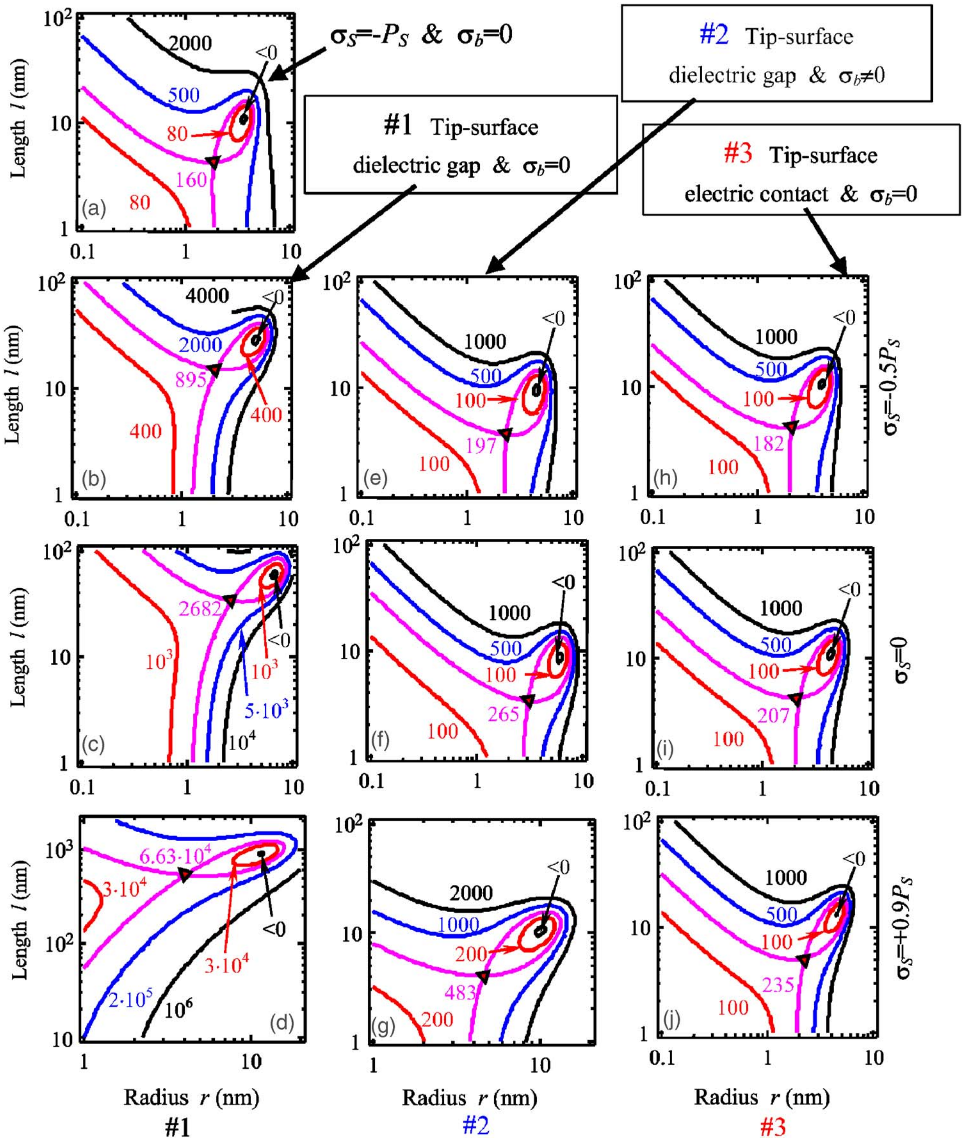

FIG. 4. (Color online) Free-energy map at critical voltage U_{cr} with increase of screening charge density, σ_S. Part (a) corresponds to the domain onset at $U_{\text{cr}} \approx 1.85$ V, $\sigma_b = 0$, and $\sigma_S = -P_S$. Left column 1 corresponds to case (ii) and $\sigma_b = 0$ for (b) $\sigma_S = -0.5 P_S$, $U_{\text{cr}} \approx 3.06$ V; (c) $\sigma_S = 0$, $U_{\text{cr}} = 6.13$ V; and (d) $\sigma_S = +0.9 P_S$, $U_{\text{cr}} = 471$ V. Central column 2 corresponds to case (ii) and $\sigma_b = -(P_S + \sigma_S)$ for (e) $\sigma_S = -0.5 P_S$, $U_{\text{cr}} \approx 1.90$ V; (f) $\sigma_S = 0$, $U_{\text{cr}} \approx 2.09$ V; and (g) $\sigma_S = +0.9 P_S$, $U_{\text{cr}} = 12.80$ V. Right column 3 corresponds to case (i) and $\sigma_b = 0$ for (h) $\sigma_S = -0.5 P_S$, $U_{\text{cr}} \approx 1.61$ V; (i) $\sigma_S = 0$, $U_{\text{cr}} \approx 1.44$ V; and (j) $\sigma_S = +0.9 P_S$, $U_{\text{cr}} = 1.38$ V. Figures near the contours are free-energy values in $k_B T$. Triangles denote saddle point (nuclei sizes). Material parameters are $P_S \approx 0.5$ C/m^2, domain wall surface energy $\psi_S \approx 50$ mJ/m^2, $\kappa = 507$, $\gamma \approx 1$, and $R_d \approx 500$ nm correspond to PZT-6B ceramics; effective distance $d \approx 8$ nm.

[case (ii)] but the domain sidewall surface screening is absent ($\sigma_b \equiv 0$), is illustrated in the left column, 1. The central column, 2, illustrates the scenario in which $\sigma_b = -(P_S + \sigma_S)$. Further decrease of $\sigma_b \leq -(P_S + \sigma_S)$ leads to the appearance of surface domain state with $l \to 0$, since interaction energy Eq. (4) becomes negative at $l = 0$. In both limiting cases $\sigma_b \equiv 0$ and $\sigma_b = -(P_S + \sigma_S)$ the screening charge density σ_S controls the domain formation, but case 2 corresponds to the much smaller critical voltage, domain length, and activation barrier at the same σ_S values.

Charge screening ($\sigma_S > +P_S$) results in a decrease of the dragging electrostatic force caused by the charged probe. As a result the critical voltage, domain length, and activation barrier increase with surface charge density changing from $-P_S$ to $+P_S$. Remarkably, the free energy is always positive at $\sigma_S = +P_S$ and $U > 0$, rendering domain nucleation impossible at $\sigma_S \to P_S$, since the depolarization energy and domain wall surface energy are always positive. This analysis illustrates that efficient surface screening is a necessary condition for domain nucleation in PFM, in agreement with studies by Gerra *et al.* illustrating the role of electrode interface on domain nucleation.[76]

The contour maps of free energy [Eq. (3)] without the screening charge σ_S redistribution energy $\Delta\Phi_\sigma$ [case (i)], corresponding to nucleation below the conductive tip or in the presence of surface electrochemical processes, are presented in the right column, 3. In contrast to case (ii), the critical bias U_{cr} slightly decreases with σ_S even at $\sigma_b = 0$. Furthermore, nucleus and critical domain sizes are almost independent of screening charge density up to $\sigma_S \leq +0.9 P_S$ in case (i).

Shown in Fig. 5 are the activation energy E_a at a critical voltage U_{cr}, as well as nucleus and critical domain sizes obtained within the framework of models (i) and (ii) for different screening charge densities, σ_S. The barrier height rapidly decreases with voltage for all scenarios 1–3 from Fig. 4. Corresponding voltage dependences of activation barrier E_a at $\sigma_S = +0.9 P_S$ (solid curves) and $\sigma_S = -P_S$ (dashed curve) are presented in Fig. 5. All curves 1–3 coincide for $\sigma_S = -P_S$, as anticipated from Eqs. (3)–(6). However, the dashed curves almost coincide with the solid one calculated in model 3 for $\sigma_S = +0.9 P_S$, showing that depolarization field contribution is negligible at growth stage. The latter affects the critical point as shown in Fig. 5(b).

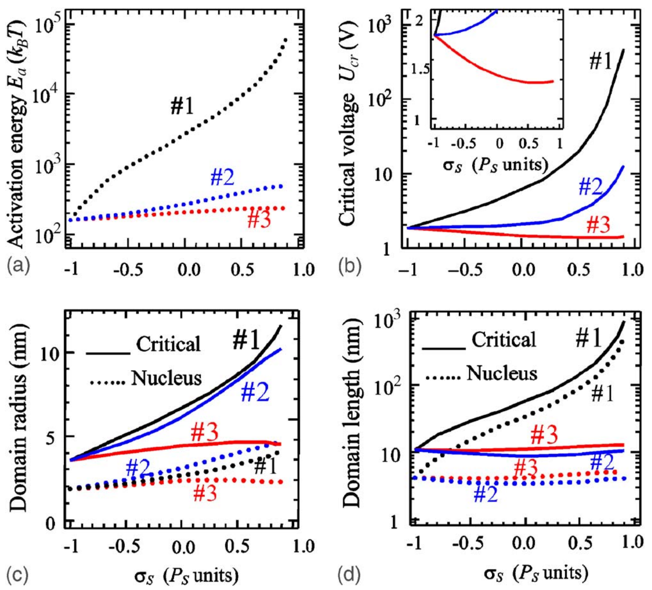

FIG. 5. (Color online) (a) Activation energy E_a calculated at critical voltage U_{cr} shown in part (b); domain nucleus and critical radius (c) and length (d) vs surface charge density σ_S calculated for PZT-6B. Material parameters and curves 1–3 description are given in caption to Fig. 3.

At $\sigma_S = -P_S$, the activation barrier for nucleation at the onset of domain stability $U = U_{cr}$ is minimal (about $200 k_B T$) and the corresponding value is close for all considered cases (see curves 1–3). It increases up to $10^5 k_B T$ for $\sigma_S \to +P_S$ along with the critical voltage for case (ii) and $\sigma_b = 0$ [see curve 1 in Figs. 5(a) and 5(b)]. The reason is the rapid increase of nucleus and critical lengths under the charge density σ_S increase from $-P_S$ to $+P_S$ [see Figs. 5(c) and 5(d)].

The kinetics of domain nucleation can be analyzed in the framework of reaction rate theory[77] assuming that the characteristic time for nucleation is $\tau = \tau_0 \exp(E_a / k_B T)$. For typical attempt time $\tau_0 = 10^{-12}$ s, the thermal activation of domain nucleation in the PFM experiment requires an activation barrier below $20 k_B T$ ($\tau \sim 10^{-3}$ s), which is impossible at $U \approx U_{cr}$ for all cases 1–3. For chosen material parameters the domains could either originate at higher voltages in the perfect ferroelectric sample [as anticipated from Fig. 6, at 5–10 V for $\sigma_S = -P_S$ or good surface screening, case (i), independently of the σ_S value], or nucleation must be defect related. Note that significantly lower barriers correspond to $BaTiO_3$ and Rochelle salt, allowing for the lower values of surface energy ($\psi_S \approx 5$ mJ/m^2 and $\psi_S \approx 0.06$ mJ/m^2, respectively).

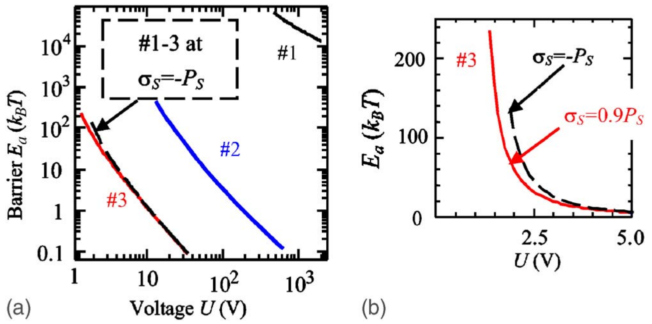

FIG. 6. (Color online) (a) Log plot of activation barrier E_a voltage dependence at $\sigma_S = +0.9 P_S$ (solid curves 1–3) in comparison with the case $\sigma_S = -P_S$, $\sigma_b = 0$ (dashed curve). (b) Linear plot shows curve 3 at $\sigma_S = +0.9 P_S$ for small voltages. Material parameters and curves 1–3 description are given in caption to Fig. 3.

For local point-charge model, for $R_d \gg r$, $r_{cr} < 2d$, and $r_{cr} < 2 l_{cr}$, expected to be valid at the onset of domain formation, we derived approximate analytical expressions for the critical voltage U_{cr}, minimal stable sizes r_{cr} and l_{cr}, and equilibrium size voltage dependence as follows:

$$U_{cr} \approx \frac{4[(\kappa+\varepsilon_e)R_d + 2\kappa d]}{(2P_S - \Delta\sigma_S)(\kappa+\varepsilon_e)R_d}\sqrt{\frac{(P_S-\sigma_S)^2 d}{3\varepsilon_0(\kappa+\varepsilon_e)}\psi_S\gamma}, \tag{7}$$

$$l_{cr}(U_{cr}) \approx 2\gamma d, \quad r_{cr}(U_{cr}) \approx \frac{\pi\sqrt{3\varepsilon_0\gamma(\kappa+\varepsilon_e)\psi_S d}}{2(P_S-\sigma_S)}, \tag{8}$$

$$r(U) \approx r_{cr}\left[1 + 2\sqrt{\frac{2d}{3r_{cr}}\left(\frac{U}{U_{cr}} - 1\right)}\right],$$

$$l(U) \approx l_{cr}\left[1 + 2\sqrt{\frac{2d}{r_{cr}}\left(\frac{U}{U_{cr}} - 1\right)}\right]. \tag{9}$$

As before, $\Delta\sigma_S = 0$ for case (i) and $\Delta\sigma_S = \sigma_S + P_S$ for case (ii). In accordance with Fig. 5 the condition $r_{cr} < 2d$ is valid for curve 2 for $-P_S \leq \sigma_S \leq 0$ and for curve 3 at all values $-P_S \leq \sigma_S \leq P_S$. Equations (7)–(9) thus define the parameters of the thermodynamically stable domains (i.e., minimum on a free-energy surface).

The barrier height and nucleus sizes (i.e., the saddle point on the free-energy surface) decrease with voltage increase as $r_S \sim U^{-1}$, $l_S \sim U^{-2}$, and $E_a \sim U^{-3}$. Approximate expressions for critical and nucleus parameters are in good qualitative agreement with numerical calculations presented by curves 2 and 3 in Figs. 5 and 6.

This analysis illustrates that the tip-surface electric contact conditions and surface screening provide critical influence on the thermodynamics of polarization switching in PFM. Specifically we obtain the following.

(a) For good tip-surface contact (nucleating domain size is smaller than tip-surface contact radius) or in the presence of efficient screening mechanisms (e.g., due to surface conductive layer or electrochemical reactions) the process is expected to be independent of the details of screening mechanism.

(b) Under the typical condition of imperfect tip-surface dielectric contact (e.g., the tip apex-sample spatial separation $\Delta R \neq 0$), variation of ambient medium from air to vacuum or inert gas, distilled water, electrolyte, and some chemically inert liquid dielectric can provide insight into surface screening effects. In particular, the dependence of critical voltage U_{cr} values over ambient conditions could clarify the surface screening influence. Remarkably, recent studies by Xue *et al.*[78] have demonstrated that values of U_{cr} on $+Z$ and $-Z$ cuts of $LiNbO_3$ or $LiTaO_3$ crystals (placed in argon ambient) differ by a factor of 2, illustrating the effect of surface state on switching mechanism.

IV. MODELING OF PIEZOELECTRIC RESPONSE

The analysis in Sec. III describes the domain evolution with bias, i.e., establishes the relationship between domain parameters and tip bias. To calculate the shape of the PFM hysteresis loop, the geometric parameters of the domain, i.e., length, l, and radius, r, must be related to the measured PFM signal. This relationship, once established, will be equally applicable to the thermodynamic theory developed in Sec. III, the kinetic theory developed by Molotskii and Shvebelman,[75,79] and for data analysis in the PFM experiment.

To establish the relationship between domain parameters and the PFM signal, we utilize the decoupled Green's function theory by Felten *et al.*[80] This approach is based on (1) the calculation of the electric field for rigid dielectric, (2) the calculation of the stress field using constitutive relations for piezoelectric materials, and (3) the calculation of the mechanical displacement field using Green's function for nonpiezoelectric elastic body. For transversally isotropic material, the tip-induced electric field can be determined using simple image charge models. For the spherical part of the tip apex, the solution is rigorous, while for the conical part of the tip an approximate line-charge model can be used.[81,82] Here, we develop the approximate expressions for piezoresponse of the initial and intermediate (cylindrical and nested cylindrical) domains for the finite Debye length of ferroelectric semiconductor.

A. Piezoresponse in the initial state with finite screening

In the decoupling approximation for transversally isotropic piezoelectric and dielectric material in the limit of weak elastic anisotropy and with finite bulk Debye length, the voltage-dependent surface displacement in the initial state is[83]

$$u_3(0) = V_Q[d_{31}f_1(\gamma,R_d) + d_{15}f_2(\gamma,R_d) + d_{33}f_3(\gamma,R_d)]. \tag{10}$$

Here V_Q is the electrostatic potential at the sample surface just below the tip, and d_{ij} are piezoelectric tensor coefficients. Functions $f_i(\gamma,R_d)$ depend on the dielectric anisotropy γ, Poisson ratio ν, screening radius R_d, and effective point charge separation d from the surface. Depending on the ratio $d/2R_d$ the following approximate expressions are derived:

$$f_3(\gamma,R_d) \approx -\frac{2\gamma\sqrt{1+(d/2R_d)^2} + 1 + (d/2R_d)^2}{[\sqrt{1+(d/2R_d)^2}+\gamma]^2}, \tag{11}$$

$$f_2(\gamma,R_d) \approx -\frac{\gamma^2}{[\sqrt{1+(d/2R_d)^2}+\gamma]^2}, \tag{12}$$

$$f_1(\gamma,R_d) \approx -\frac{2\gamma\nu\sqrt{1+(d/2R_d)^2} + (1+2\nu)[1+(d/2R_d)^2]}{[\sqrt{1+(d/2R_d)^2}+\gamma]^2}. \tag{13}$$

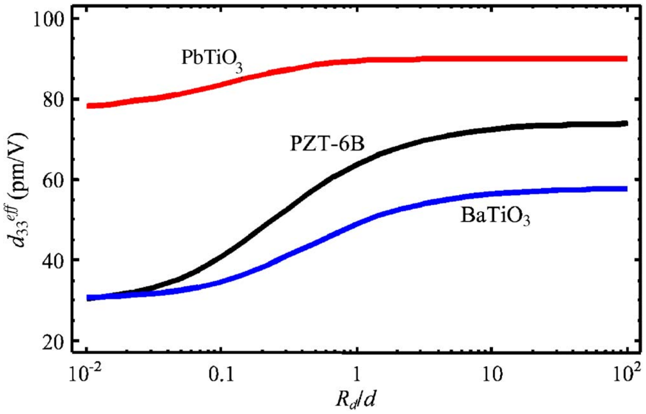

FIG. 7. (Color online) PFM response of the initial state d_{33}^{eff} vs the ratio R_d/d for $\nu=0.35$, $\gamma=1$ for ferroelectrics PbTiO$_3$, PZT-6B, and BaTiO$_3$.

The functions $f_i(\gamma,R_d)$ saturate at $R_d/d \to \infty$ (see Appendix C in Ref. 83). The saturation values $f_i(\gamma)$ correspond to the case of perfect dielectric and are given by Eqs. (11)–(13). They define the PFM response in the initial and final states of switching process.[84,85]

The PFM response $d_{33}^{\text{eff}} = u_3(0)/V_Q$ versus the ratio R_d/d is presented in Fig. 7. Note that the finite Debye length of the material, i.e., the conductivity, reduces the electromechanical response. The response does not become zero at $R_d/d \to 0$, due to the finiteness of the electric field; however, relative contributions of piezoelectric constants to overall response change.

Experimentally, PFM images are often obtained for materials with large leakage and semiconductive perovskites such as BaTiO$_3$ termistors, or piezoelectric semiconductors such as III-V nitrides and ZnO. The practical limitation for PFM measurements in conductive materials is thus potential drops in the tip-surface junction due to the finite conductivity and, at high current densities, thermal degradation of tip and surface materials.

B. Piezoresponse in the intermediate states

For the intermediate state of the switching process, i.e., ferroelectric domain in the matrix with antiparallel polarization orientation, Eq. (10) can be rewritten as

$$\begin{aligned} u_3^i = V_Q[&d_{31}g_1(\gamma,R_d,r,l) + d_{15}g_2(\gamma,R_d,r,l) \\ &+ d_{33}g_3(\gamma,R_d,r,l)], \end{aligned} \tag{14a}$$

$$g_i(\gamma,R_d,r,l) = f_i(\gamma,R_d) - 2w_i(\gamma,R_d,r,l). \tag{14b}$$

Functions $w_i=0$ in the initial and $w_i=f_i$ in the final state of the switching process. For perfect dielectric $R_d \to \infty$, the functions $w_i(\gamma,\nu,R_d,r,l) \equiv w_i^{\infty}(r,l,d)$ are dependent primarily on the domain sizes r and l and effective charge-surface separation d. Note that in a typical PFM experiment the domains are elongated, $l \gg r$, while the tip-induced electric field is concentrated in the near-surface region. Hence, domain shape can often be approximated as a semi-infinite cylinder. For arbitrary rotationally invariant domain shape, the integral expressions for $w_i^{\infty}(r,l,d)$ are listed in Ref. 55.

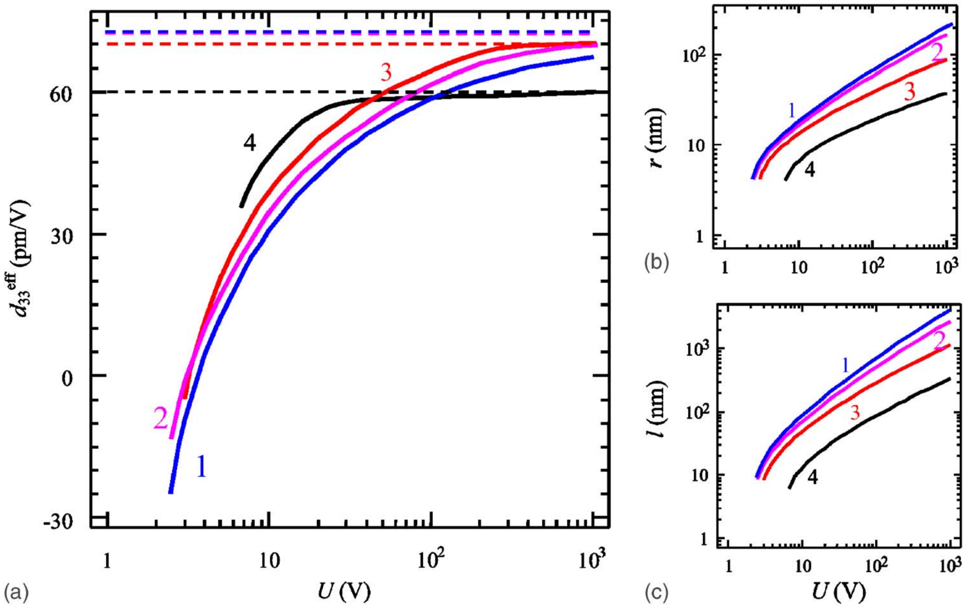

FIG. 8. (Color online) Effective piezoresponse (a) in the intermediate state of switching process and corresponding domain radius (b) and length (c) voltage dependence at different R_d radii: ∞ (curve 1), 500 nm (curve 2), 50 nm (curve 3), and 5 nm (curve 4). Dashed curves denote piezoresponse saturation values. Material parameters: $R_0=50$ nm, $\varepsilon_e=81$, others correspond to Fig. 3, and $\sigma_S=-P_S$.

For more complex tip geometries and $R_d \to \infty$, Eqs. (14a) and (14b) could be summed over corresponding image charge series to yield the response for tips with complex geometries. For ferroelectric-semiconductor with finite Debye screening radius, R_d, the functions $w_i(\gamma,R_d,r,l)$ have the form of extremely cumbersome irreducible threefold integrals that should be evaluated numerically. Here we derive closed-form expressions for the particular case of a cylindrical domain or a prolate semiellipsoid $(r \ll l)$. In this case, the functions w_i are almost independent of the domain length and can be approximated as

$$w_3(\gamma,R_d,r) \approx \frac{f_3(\gamma,R_d)\sqrt{1+(d/R_d)^2}(r/d)}{\sqrt{1+(d/R_d)^2}(r/d)+B_3(\gamma)/|f_3(\gamma,R_d)|}, \quad (15)$$

$$w_2(\gamma,R_d,r) \approx \frac{f_2(\gamma,R_d)\sqrt{[1+(d/R_d)^2]^3}(r/d)}{\sqrt{[1+(d/R_d)^2]^3}(r/d)+B_2(\gamma)/|f_2(\gamma,R_d)|}, \quad (16)$$

$$w_1(\gamma,R_d,r) \approx (1+2\nu)w_3(\gamma,R_d,r) - \frac{2(1+\nu)}{\gamma}\sqrt{1+\left(\frac{d}{2R_d}\right)^2}\,w_2(\gamma,R_d,r). \quad (17)$$

The constants $B_i(\gamma)$ depend solely on the dielectric anisotropy of material and are given in Ref. 86, e.g., $B_1(1)=\pi/16$ and $B_3(1)=B_2(1)=3\pi/32$. For large domain sizes, the response [Eqs. (15)–(17)] in the intermediate states saturates as d/r for $R_d \to \infty$ (perfect dielectric), whereas for finite Debye radii the saturation is faster and the response scales as $R_d d/r^2$.

Effective piezoresponse in the intermediate state of the switching process and the corresponding domain radius and length voltage dependence are shown in Fig. 8 for different R_d. It is clear from Figs. 8(b) and 8(c) that the domain sizes decrease with decreasing R_d. Despite this, the piezoresponse saturates much more quickly at small values $R_d \leqslant 10$ nm than at large ones $R_d \geqslant 10^3$ nm.

The reason for the faster response saturation is that the tip potential quickly vanishes for small R_d leading to a strong decrease of the PFM response region $(R_{\max}, h_{\max})$. The space outside the region $(R_{\max}, h_{\max})$ is invisible to PFM, so when the domain radius reaches $R_{\max}$ and height acquires $h_{\max}$, respectively, the response almost saturates.

Note that materials such as perfect $BiFeO_3$, $LiNbO_3$, $LiTaO_3$, or $BaTiO_3$ crystals typically possess $R_d > 1$ μm, while the slightly doped or defect ones have $R_d \sim 100$ nm. Thus the Debye screening effect on the nanodomain nucleation and early stages of radial growth is expected to be relatively weak. However, it will significantly affect the vertical domain growth (since $l \gg R_d$ is possible) and lateral size saturation at high voltages, resulting in self-limiting behavior due to tip field screening.

C. Modeling loop shape in weakly pinned limit

In this section we analyze the shape of piezoresponse loop for lead zirconate titanate (PZT) in the weak pinning limit. To calculate the thermodynamic hysteresis loop shape from the bias dependence of the domain size, we assume that the domain evolution follows the equilibrium domain size on the forward branch of the hysteresis loop [see Fig. 2(c)]. Corresponding piezoelectric loops calculated using thermodynamic parameters derived in Sec. III are shown in Figs. 9 and 10. The initial domain nucleation occurs at $U \geqslant U_{\rm cr}$ (path 12). Then domain sizes increase under the further voltage increase (path 23). On the reverse branch of the hysteresis loop, the domain does not shrink. Rather, the domain wall is pinned by the lattice and defect (path 34).[42] The inverted domain appeared only at $U \leqslant -U_{\rm cr}$ (path 45). A sufficiently 'big" domain acts as a matrix for the inverted one, appearing just below the tip at $U \leqslant -U_{\rm cr}$ (paths 45 and 56). The inverted domain size increases with further voltage decrease (path 56). At point 6, the domain walls annihilate and the system returns to the initial state (path 61). We refer to the scenario

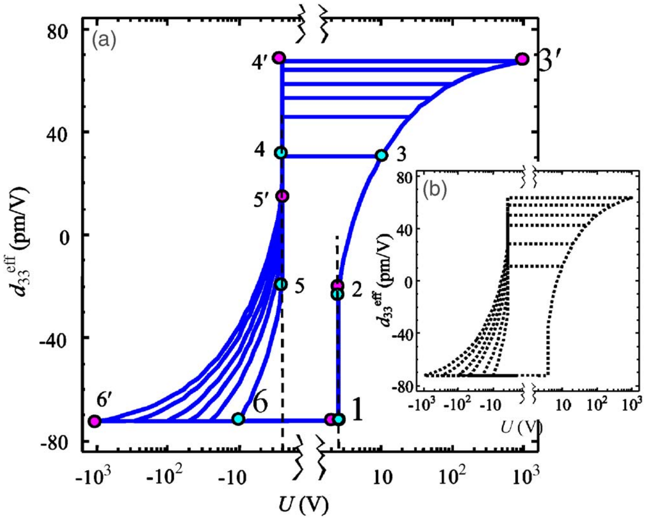

FIG. 9. (Color online) Piezoelectric response as the function of applied voltage for PZT-6B at different maximal voltages 10, 25, 40, 100, 200, and 10^3 V. Solid curves (a) represent local point-charge approximation of the tip; almost the same dotted ones (b) correspond to the exact series for sphere-tip interaction energy. Material parameters and tip-surface characteristics are given in Fig. 3; $d_{33}=74.94$ pm/V, $d_{31}=-28.67$ pm/V, and $d_{15}=135.59$ pm/V, $\sigma_S=-P_S$.

in which the domain size closely follows the thermodynamic model on forward bias, and domain wall does not move on reverse bias, due to weak pinning.

Note that for unsaturated response the loops possess intrinsic vertical asymmetry (downward shift) even in the absence of the regions with frozen polarization. This follows from the fact that the response of the nested domains (path 56) differs from the single one (paths 1–3). Domain walls annihilate in point 6, then response coincides with the one from the initial state (paths 4–0). The loop vertical asymmetry decreases under the maximal voltage increase, namely, the loop 1-2-3-4-5-6 that corresponds to the maximal voltage of 10 V is strongly asymmetrical, whereas the loop 1-2-3-4′-5′-6 that corresponds to the maximal voltage of 10^3 V becomes almost symmetrical.

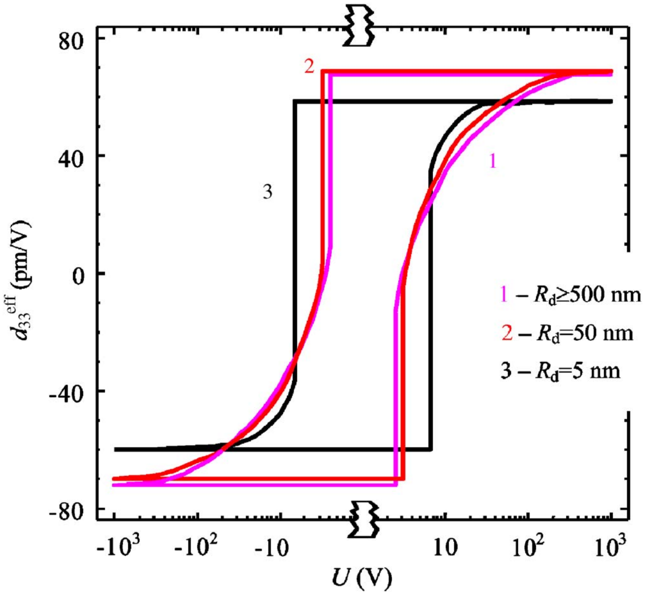

FIG. 10. (Color online) Piezoelectric response as the function of applied voltage at different R_d radii: ≥500 nm (curve 1), 50 nm (curve 2) and 5 nm (curve 3). Point-charge model with $R_0=50$ nm, material parameters corresponding to PZT-6B and $\sigma_S=-P_S$.

The influence of Debye screening radius R_d on piezoelectric response is shown in Fig. 10. Despite the decrease of equilibrium domain sizes the piezoresponse saturates much more quickly at small R_d values (about 30 V for $R_d=5$ nm) than at big ones (about 1 kV for $R_d=500$ nm). This effect is due to the quick vanishing of the tip potential at small R_d radii (see Sec. IV B).

To summarize, the effects of domain surface screening and bulk Debye screening on piezoresponse loop shape, coercive voltage, and saturation rate are the following.

(a) The surface screening strongly influences the domain nucleation and initial growth stages. The coercive voltage (loop width) and nucleation voltages are controlled by σ_S value (see Sec. III). At the same time, piezoresponse weakly depends on σ_S at high voltages, i.e., surface screening does not affect the saturation law.

(b) The Debye screening radius R_d strongly influences the piezoresponse at high voltages and thus determines the saturation law (i.e., high-voltage tails of hysteresis loop), whereas nucleation voltage depends on R_d relatively weakly.

Thus, the effect of surface and Debye screening on piezoresponse loop shape is complementary with respect to nucleation and loop saturation behavior.

V. COMPARISON WITH EXPERIMENT

Shown in Fig. 11(a) is the typical hysteresis loops obtained from a multiferroic bismuth ferrite 240 nm thick epitaxial film. Symbols are experimental saturated hysteresis loops for three different maximal voltages $U_{\rm max}=5,10,15$ V. Note the presence of hysteretic (forward and reverse branches are different) and saturated (forward and reverse branches saturate) parts of the loop. The nucleation event is clearly visible. Below the nucleation bias ($U_{\rm max}<5$ V), the switching does not proceed, while above nucleation bias the loop opens up. The vertical asymmetry of the loops (bias dependent downward shift) is explained in Fig. 11(b) (see also Fig. 9), evidencing the role of pinning on the switching process.

Dashed loops in Fig. 11(a) were calculated from Eqs. (7)–(9) at $\Delta\sigma_S=\sigma_S+P_S$ and Eq. (14) for the prolate domain with $l \gg r$ at $\rm BiFeO_3$ material parameters: polarization $P_S \approx 0.51$ C/m^2, effective dielectric constant $\kappa=85$, anisotropy $\gamma \approx 1$, and piezoelectric coefficients $d_{33}=26$ pm/V, $d_{31}=-12$ pm/V, and $d_{15}=4$ pm/V.[87] At voltages $U>10$ V theoretical hysteresis loops saturate much more slowly in comparison with experimental ones.

Shown in Fig. 11(c) is domain radius versus applied voltage. Symbols correspond to the deconvolution of experimental loops (a) based on Eqs. (14a) and (14b) for the prolate domain with $l \gg r$, namely,

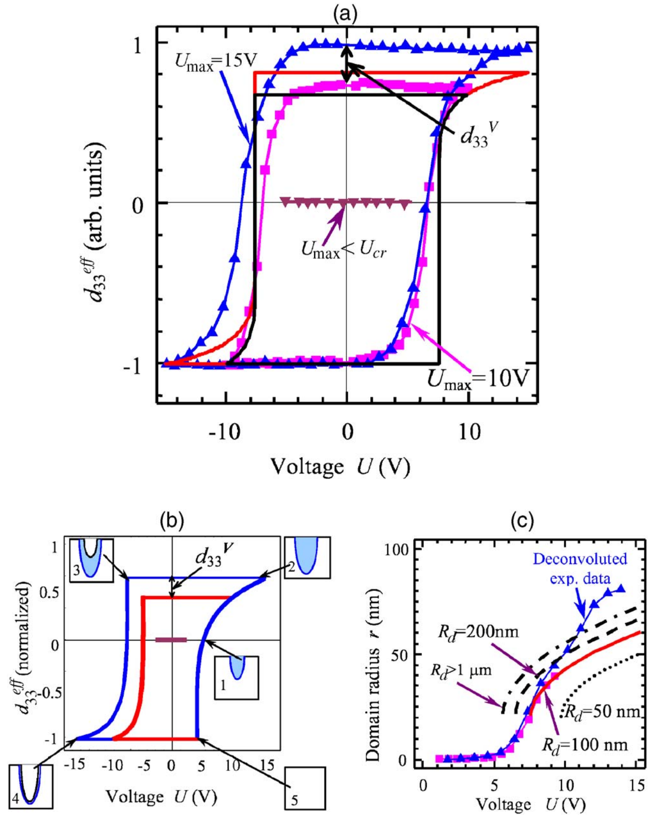

FIG. 11. (Color online) (a) Typical piezoresponse loops obtained for epitaxial 200 nm thick BiFeO$_3$ film (sample courtesy of T. Zhao and R. Ramesh, UC Berkeley). Joined together down triangles, squares, and up triangles are experimental data for the three different maximal voltages $U_{\max}=5, 10, 15$ V. Corresponding solid curves were calculated for BiFeO$_3$ material parameters, effective charge-surface separation $d \approx 30$ nm, and fitting parameters $R_d \sim 100$ nm, $\psi_S \approx 200$ mJ/m^2, $\varepsilon_e=51$, and $\sigma_S=0.6P_S$. (b) Schematics explaining piezoresponse loops asymmetry. (c) Domain radius via applied voltage: symbols correspond to the deconvolution of loops (a) from Eqs. (14a) and (14b); solid, dashed, dash-dotted, and dotted curves were calculated from Eqs. (7)–(9) for BiFeO$_3$ material with different R_d values listed near the curves.

$$d_{33}^{\text{eff}}(r) \approx -\left(\frac{3}{4}d_{33} + \frac{1+4\nu}{4}d_{31}\right)\frac{\pi d - 8r}{\pi d + 8r} - \frac{d_{15}}{4}\frac{3\pi d - 8r}{3\pi d + 8r}. \tag{18}$$

Theoretical curves were calculated from Eqs. (7)–(9) for different R_d values, with all other BiFeO$_3$ material parameters being the same.

Effective charge-surface separation $d \approx 30$ nm was obtained from the tip calibration procedure based on domain wall profile fitting and described in detail in Ref. 88. In accordance with relation $d=\varepsilon_e R_0/\kappa$ valid in effective point-charge model, the value $d \approx 30$ nm corresponds to the ambient dielectric constant $\varepsilon_e=51$ at tip nominal curvature $R_0=50$ nm. Then the domain wall surface energy $\psi_S \approx 200$ mJ/m^2, surface charge density $\sigma_S \approx +0.6P_S$, and screening radius $R_d \approx 100$ nm were chosen to fit the experimental nucleation voltage 7.5 V, piezoresponse curves tilt at small voltages, and critical domain radius 20 nm obtained from piezoresponse loop deconvolution [see Figs. 11(a) and 11(c)]. It is clear from Fig. 11(c) that estimation $R_d \approx 100–200$ nm corresponds to the best fitting of experimental data. This value is in agreement with the estimation $R_d \approx 0.1–1$ μm from the formulaes $R_d=\sqrt{\varepsilon_{11}\varepsilon_0 k_B T/(e^2 n_d)}$ (T is absolute temperature and k_B is Boltzmann's constant), using permittivity $\varepsilon_{11}=70$ obtained from independent dielectric measurements and carrier concentration $n_d \sim 10^{14}-10^{16}$ cm^{-3} extracted from the conductivity measurements of the same bismuth ferrite (BFO) films at room temperature.[89]

Note that in most cases, the bias required for nucleation is of the order of 5–20 V. Similar hysteresis loops are observed for other ferroelectric materials, including PZT,[44] strontium-bismuth titanate (SBT),[37,45] etc.

VI. DISCUSSION

In further discussion of the agreement between theoretical and experimental results, we focus on two aspects, namely, (I) nucleation bias and (II) overall loop shape.

Experimentally measured values of nucleation bias are determined by the activation energy for nucleation that decreases rapidly with applied bias. For experimentally measured values of 5–10 V the radius of critical nucleus and corresponding activation energies are of the order of 1–0.5 nm and 0.25–0.5 eV, respectively, within the local point-charge model framework. The corresponding nucleation times are $\tau=2-2\times10^{-5}$ s, making thermally activated thermodynamic nucleation feasible even on ideal surface in the absence of defects.

The most remarkable feature of the theoretical hysteresis loops in the weak pinning regime is that they are predicted to be extremely narrow and saturate rather slowly in ferroelectrics with large Debye lengths ($R_d/r \gg 1$). This behavior follows from the $1/r$ dependence of Green's function in 3D case, implying that the PFM signal will saturate to 90% of its final value when the domain diameter achieves ten times the characteristic tip size (i.e., charge-surface separation in the point-charge model, or tip radius in the sphere-plane one).

Note that in an elegant study by Kholkin *et al.*[30] domains imaged at different stages of the hysteresis loop illustrate that saturation is achieved only for domains of order of 200–300 nm, well above the tip size that can be estimated from the spatial resolution as ~20–30 nm.

Experimentally obtained hysteresis loops nearly always demonstrate much faster saturation than the loops predicted from thermodynamic theory [compare symbols and dashed curves in Fig. 11(a)]. This behavior can be ascribed to several possible mechanisms, including (a) delayed domain nucleation (compared to thermodynamic model) due to poor tip-surface contact that leads to rapid jump from initial to final state, (b) finite conductivity and faster decay of electrostatic fields in the material, (c) kinetic effects on domain wall motion, and (d) surface screening and charge injection effects.

(a) *Delayed nucleation*. The activation barrier for nucleation is extremely sensitive to maximal electric field in the tip-surface junction region, which can be significantly reduced by surface adsorbates, quantum effects due to finite Thomas-Fermi length in tip material, polarization suppression at surfaces, etc. These factors are significantly less important for determining the fields at

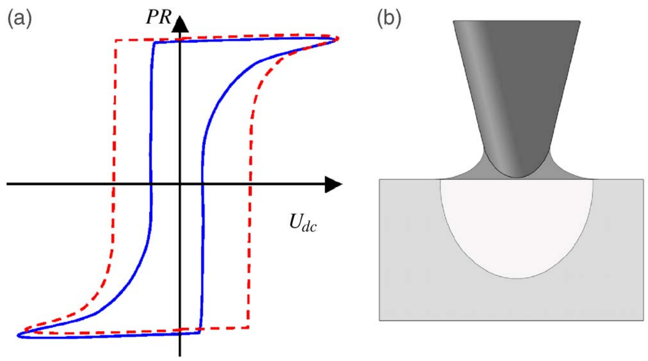

FIG. 12. (Color online) (a) Delayed nucleation will result in the broadening of the low-bias part of the hysteresis loop, effectively resulting in faster saturation. (b) The presence of the conductive water meniscus at the tip-surface junction effectively broadens the radius of electrical tip-surface contact, while mechanical contact remains unaffected.

larger separation from contact, and hence affect primarily domain nucleation, rather than subsequent domain wall motion. This effect will result in sudden onset of switching, increasing the nucleation bias and rendering the loop squarer (see Fig. 12).

(b) *Conductivity and finite Debye length*. The second possible explanation for the observed behavior is finite conductivity of the sample and/or surrounding medium. In this case, screening by free carriers will result in crossover from power law to exponential decay of electrostatic fields on the depth comparable to the Debye length. This was shown to result in self-limiting effect in domain growth.[26,70] Given that in most materials studied to date Debye lengths are of the order of microns, this explanation cannot universally account for experimental observation.

(c) *Domain wall motion kinetics*. In realistic material, domain growth will be affected by the kinetics of domain wall motion. In the weak pinning regime, the domain size is close to the thermodynamically predicted, while in kinetic (strong pinning) regime the domain is significantly smaller. Both domain length and radius will grow slower than predicted by thermodynamic model. The pinning is likely to broaden hysteresis loop compared to thermodynamic shape.

(d) *Surface conductivity effect*. The presence of extrinsic conductive water layer can significantly affect electric conditions on the ferroelectric surface. The surface charging due to lateral diffusion of charged species can result in rapid broadening of the domain in radial direction, i.e., electrical radius of tip-surface contact grows with time. Given that only the part of the surface in contact with the tip results in cantilever deflection (i.e., electrical radius is much larger than mechanical radius), this will result in rapid saturation of the hysteresis loop.

To summarize, the existing data suggest that experimental results and theoretical models can be reconciled only if the radius of electrical contact is significantly larger than the radius of mechanical contact. Also we could expect that piezoresponse hysteresis loop shape (nucleation bias and saturation rate) is dependent upon ambient humidity or surface charges migration ubiquitous on oxide surfaces. Possible dependence of critical voltage U_{cr} values over ambient conditions between the probe apex and sample surface (surface orientation with respect to the crystallographic axes, vacuum or inert gas, distilled water, electrolyte, and some chemically inert liquid dielectric) could clarify the surface screening influence. Thus, further purposeful experimental justification of the prediction and detailed quantitative study is desirable.

VII. CONCLUSIONS

The hysteresis loop formation mechanism in PFM is analyzed in detail. The role of surface charges and finite Debye length on the thermodynamics of the switching process is elucidated. The general formalism relating parameters of domain to PFM signal is developed. This analysis is general and is applicable for modeling of arbitrary switching mechanisms, as well as for quantitative interpretation of PFS data. We demonstrated that the effects of surface charges and Debye screening on piezoresponse loop are complementary with respect to domain nucleation and loop saturation behavior as follows.

(a) Surface screening charges strongly influence the domain nucleation and initial stage of growth, whereas affect the high-voltage tail of hysteresis loop only weakly.

(b) The value of Debye screening radius strongly influences the piezoresponse behavior at high voltages and so determines the saturation law, whereas nucleation voltage is affected relatively weakly.

Comparison with experimental data indicates that experimental hysteresis loops saturate much faster than predicted by thermodynamic theory. The possible factors explaining this behavior, including domain wall pinning, finite conductivity, delayed nucleation, and surface charging, are considered. Based on the comparison of experimental data and theoretical prediction, we believe that polarization-switching processes are strongly mediated by the diffusion of surface charges generated in the tip-surface contact area. Surface charging increases the area of electrical contact, resulting in faster loop saturation, and also can account for experimentally observed logarithmic domain growth kinetics [e.g., observed for two-dimensional (2D) diffusion of molecular species on surfaces].[90] In this mechanism, the domain size effectively follows the 2D screening charge patch. Due to different time scales, the charges are unlikely to affect PFM imaging.

Finally, the analysis developed in this paper can be further extended for the description of polarization switching in the vicinity of the defects and local switching centers. The defect-induced lowering of the activation energy for domain nucleation can be directly determined from the local nucleation bias, and corresponding defect parameters can be determined using the mathematical formalism above.

ACKNOWLEDGMENTS

Research supported in part (S.V.K., B.J.R., and S.J.) by Oak Ridge National Laboratory, managed by UT-Battelle, LLC, for the U.S. Department of Energy under Contract No. DE-AC05-00OR22725.

[1] J. F. Scott, *Ferroelectric Memories* (Springer, Berlin, 2000).
[2] *Nanoscale Characterization of Ferroelectric Materials*, edited by M. Alexe and A. Gruverman (Springer, New York, 2004).
[3] *Nanoscale Phenomena in Ferroelectric Thin Films*, edited by S. Hong (Kluwer, Dordrecht, 2004).
[4] S. V. Kalinin, D. A. Bonnell, T. Alvarez, X. Lei, Z. Hu, J. H. Ferris, Q. Zhang, and S. Dunn, Nano Lett. **2**, 589 (2002).
[5] J. F. Scott, F. D. Morrison, M. Miyake, P. Zubko, X. Lou, V. M. Kugler, S. Rios, M. Zhang, T. Tatsuta, O. Tsuji, and T. J. Leedham, J. Am. Ceram. Soc. **88**, 1691 (2005).
[6] M. Dawber, K. M. Rabe, and J. F. Scott, Rev. Mod. Phys. **77**, 1083 (2005).
[7] S. K. Streiffer, J. A. Eastman, D. D. Fong, C. Thompson, A. Munkholm, M. V. Ramana Murty, O. Auciello, G. R. Bai, and G. B. Stephenson, Phys. Rev. Lett. **89**, 067601 (2002).
[8] C. H. Ahn, K. M. Rabe, and J.-M. Triscone, Science **303**, 488 (2004).
[9] P. Ghosez and J. Junquera, in *First-Principles Modeling of Ferroelectric Oxides Nanostructures*, Handbook of Theoretical and Computational Nanotechnology, Chap. 134, edited by M. Rieth and W. Schommers (American Scientific Publisher, Stevenson Ranch, 2006).
[10] S. Ducharme, V. M. Fridkin, A. V. Bune, S. P. Palto, L. M. Blinov, N. N. Petukhova, and S. G. Yudin, Phys. Rev. Lett. **84**, 175 (2000).
[11] A. A. Gorbatsevich and Yu. V. Kopaev, Ferroelectrics **161**, 321 (1994).
[12] I. I. Naumov, L. Bellaiche, and H. X. Fu, Nature (London) **432**, 737 (2004).
[13] P. Günther and K. Dransfeld, Appl. Phys. Lett. **62**, 1137 (1992).
[14] K. Franke, J. Besold, W. Haessler, and C. Seegebarth, Surf. Sci. Lett. **302**, L283 (1994).
[15] A. Gruverman, O. Auciello, and H. Tokumoto, J. Vac. Sci. Technol. B **14**, 602 (1996).
[16] T. Hidaka, T. Maruyama, M. Saitoh, N. Mikoshiba, M. Shimizu, T. Shiosaki, L. A. Wills, R. Hiskes, S. A. Dicarolis, and J. Amano, Appl. Phys. Lett. **68**, 2358 (1996).
[17] X. Zhang, D. Xue, X. Liu, and K. Kitamura, Physica B **387**, 147 (2007).
[18] Y. Cho, S. Hashimoto, N. Odagawa, K. Tanaka, and Y. Hiranaga, Nanotechnology **17**, S137 (2006).
[19] M. Damjanovic, in *Hysteresis in Piezoelectric and Ferroelectric Materials*, The Science of Hysteresis Vol. 3, edited by I. Mayergoyz and G. Bertolli (Elsevier, New York, 2005).
[20] Y. Ishibashi and H. Orihara, Integr. Ferroelectr. **9**, 57 (1995).
[21] R. Waser, U. Bottger, and M. Grossman, Top. Appl. Phys. **93**, 31 (2004).
[22] M. Abplanalp, Dr. Nat. Sci. thesis, Swiss Federal Institute of Technology, 2001.
[23] M. Molotskii, J. Appl. Phys. **93**, 6234 (2003).
[24] S. V. Kalinin, A. Gruverman, B. J. Rodriguez, J. Shin, A. P. Baddorf, E. Karapetian, and M. Kachanov, J. Appl. Phys. **97**, 074305 (2005).
[25] A. Yu. Emelyanov, Phys. Rev. B **71**, 132102 (2005).
[26] A. N. Morozovska and E. A. Eliseev, Phys. Rev. B **73**, 104440 (2006).
[27] A. Gruverman and A. L. Kholkin, Rep. Prog. Phys. **69**, 2443 (2006).
[28] R. Landauer, J. Appl. Phys. **28**, 227 (1957).
[29] A. Gruverman, B. J. Rodriguez, C. Dehoff, J. D. Waldrep, A. I. Kingon, R. J. Nemanich, and J. S. Cross, Appl. Phys. Lett. **87**, 082902 (2005).
[30] A. L. Kholkin, I. K. Bdikin, V. V. Shvartsman, A. Orlova, D. Kiselev, A. A. Bogomolov, and S.-H. Kim, in *Scanning-Probe and Other Novel Microscopies of Local Phenomena in Nanostructured Materials*, edited by S. V. Kalinin, B. Goldberg, L. M. Eng, and B. D. Huey (Mater. Res. Soc. Symp. Proc. **838E**, Warrendale, PA, 2005), p. O7.6.
[31] T. Tybell, P. Paruch, T. Giamarchi, and J.-M. Triscone, Phys. Rev. Lett. **89**, 097601 (2002).
[32] P. Paruch, T. Giamarchi, and J.-M. Triscone, Phys. Rev. Lett. **94**, 197601 (2005).
[33] M. Dawber, A. Gruverman, and J. F. Scott, J. Phys.: Condens. Matter **18**, L71 (2006).
[34] A. Agronin, Y. Rosenwaks, and G. Rosenman, Appl. Phys. Lett. **88**, 072911 (2006).
[35] H. Birk, J. Glatz-Reichenbach, L. Jie, E. Schreck, and K. Dransfeld, J. Vac. Sci. Technol. B **9**, 1162 (1991).
[36] I. D. Kim, Y. Avrahami, H. L. Tuller, Y. B. Park, M. J. Dicken, and H. A. Atwater, Appl. Phys. Lett. **86**, 192907 (2005).
[37] S. V. Kalinin, A. Gruverman, and D. A. Bonnell, Appl. Phys. Lett. **85**, 795 (2004).
[38] L. M. Eng, H.-J. Güntherodt, G. A. Schneider, U. Köpke, and J. Muñoz Saldaña, Appl. Phys. Lett. **74**, 233 (1999).
[39] L. M. Eng, H.-J. Güntherodt, G. Rosenman, A. Skliar, M. Oron, M. Katz, and D. Eger, J. Appl. Phys. **83**, 5973 (1998).
[40] B. J. Rodriguez, A. Gruverman, A. I. Kingon, R. J. Nemanich, and J. S. Cross, J. Appl. Phys. **95**, 1958 (2004).
[41] R. Desfeux, C. Legrand, A. Da Costa, D. Chateigner, R. Bouregba, and G. Poullain, Surf. Sci. **600**, 219 (2006).
[42] S. Jesse, A. P. Baddorf, and S. V. Kalinin, Appl. Phys. Lett. **88**, 062908 (2006).
[43] Y. Saya, S. Watanabe, M. Kawai, H. Yamada, and K. Matsushige, Jpn. J. Appl. Phys., Part 1 **39**, 3799 (2000).
[44] M. Alexe, C. Harnagea, D. Hesse, and U. Gosele, Appl. Phys. Lett. **79**, 242 (2001).
[45] C. Harnagea, A. Pignolet, M. Alexe, D. Hesse, and U. Gosele, Appl. Phys. A: Mater. Sci. Process. **70**, 261 (2000).
[46] D. Ricinschi, L. Mitoseriu, A. Stancu, P. Postolache, and M. Okuyama, Integr. Ferroelectr. **67**, 103 (2004).
[47] D. Ricinschi, M. Noda, M. Okuyama, Y. Ishibashi, M. Iwata, and L. Mitoseriu, J. Korean Phys. Soc. **42**, S1232 (2003).
[48] D. Ricinschi and M. Okuyama, Integr. Ferroelectr. **50**, 159 (2002).
[49] A. Gruverman, B. J. Rodriguez, A. I. Kingon, R. J. Nemanich, J. S. Cross, and M. Tsukada, Appl. Phys. Lett. **82**, 3071 (2003).
[50] A. Gruverman, B. J. Rodriguez, A. I. Kingon, R. J. Nemanich, A. K. Tagantsev, J. S. Cross, and M. Tsukada, Appl. Phys. Lett. **83**, 728 (2003).
[51] C. Dehoff, B. J. Rodriguez, A. I. Kingon, R. J. Nemanich, A. Gruverman, and J. S. Cross, Rev. Sci. Instrum. **76**, 023708 (2005).
[52] C. S. Ganpule, V. Nagarajan, H. Li, A. S. Ogale, D. E. Steinhauer, S. Aggarwal, E. Williams, R. Ramesh, and P. DeWolf, Appl. Phys. Lett. **77**, 292 (2000).
[53] A. Wu, P. M. Vilarinho, V. V. Shvartsman, G. Suchaneck, and A. L. Kholkin, Nanotechnology **16**, 2587 (2005).
[54] M. Molotskii, J. Appl. Phys. **97**, 014109 (2005).
[55] A. N. Morozovska, E. A. Eliseev, and S. V. Kalinin, Appl. Phys. Lett. **87**, 082902 (2005).
[56] A. N. Morozovska, S. V. Kalinin, E. A. Eliseev, and S. V. Svechnikov, Ferroelectrics **354**, 198 (2007).
[57] S. V. Kalinin and D. A. Bonnell, J. Appl. Phys. **87**, 3950 (2000).
[58] S. V. Kalinin, C. Y. Johnson, and D. A. Bonnell, J. Appl. Phys. **91**, 3816 (2002).
[59] S. V. Kalinin and D. A. Bonnell, Phys. Rev. B **63**, 125411 (2001).
[60] S. Bühlmann, E. Colla, and P. Muralt, Phys. Rev. B **72**, 214120 (2005).
[61] D. Dahan, M. Molotskii, G. Rosenman, and Y. Rosenwaks, Appl. Phys. Lett. **89**, 152902 (2006).
[62] A. L. Kholkin, I. K. Bdikin, V. V. Shvartsman, and N. A. Pertsev, Nanotechnology **18**, 095502 (2007).
[63] S. V. Kalinin and D. A. Bonnell, Nano Lett. **4**, 555 (2004).
[64] S. V. Kalinin, J. Shin, S. Jesse, D. Geohegan, A. P. Baddorf, Y. Lilach, M. Moskovits, and A. Kolmakov, J. Appl. Phys. **98**, 044503 (2005).
[65] S. Cunningham, I. A. Larkin, and J. H. Davis, Appl. Phys. Lett. **73**, 123 (1998).
[66] V. M. Fridkin, *Ferroelectric Semiconductors* (Consultant Bureau, New York, 1980).
[67] P. Paruch, T. Tybell, and J.-M. Triscone, Appl. Phys. Lett. **79**, 530 (2001).
[68] The linear theory is expected to be applicable everywhere except the immediate vicinity of the domain wall with uncompensated bound charge. The effective interface charge will be reduced by band bending and ferroelectric nonlinearity on the effective value σ_b.
[69] A. N. Morozovska, S. V. Svechnikov, E. A. Eliseev, and S. V. Kalinin, Phys. Rev. B **76**, 054123 (2007).
[70] A. N. Morozovska and E. A. Eliseev, Phys. Status Solidi B **243**, 1996 (2006).
[71] J. Padilla, W. Zhong, and D. Vanderbilt, Phys. Rev. B **53**, R5969 (1996).
[72] V. Gopalan, T. E. Mitchell, and K. E. Sickafus, Integr. Ferroelectr. **22**, 405 (1998).
[73] T. J. Yang and U. Mohideen, Phys. Lett. A **250**, 205 (1998).
[74] D. A. Scrymgeour, V. Gopalan, A. Itagi, A. Saxena, and P. J. Swart, Phys. Rev. B **71**, 184110 (2005).
[75] M. Molotskii and M. Shvebelman, Ferroelectrics **301**, 67 (2004).
[76] G. Gerra, A. K. Tagantsev, and N. Setter, Phys. Rev. Lett. **94**, 107602

(2005).

[77] P. Hanggi, P. Talkner, and M. Borkovec, Rev. Mod. Phys. **62**, 251 (1990).

[78] D. Xue, S. Wu, Y. Zhu, K. Terabe, K. Kitamura, and J. Wang, Chem. Phys. Lett. **377**, 475 (2003).

[79] M. Molotskii and M. Shvebelman, Philos. Mag. **85**, 1637 (2005).

[80] F. Felten, G. A. Schneider, J. Munoz Saldana, and S. V. Kalinin, J. Appl. Phys. **96**, 563 (2004).

[81] S. V. Kalinin and D. A. Bonnell, Phys. Rev. B **65**, 125408 (2002).

[82] S. Belaidi, P. Girard, and G. Leveque, J. Appl. Phys. **81**, 1023 (1997).

[83] A. N. Morozovska, S. V. Svechnikov, E. A. Eliseev, S. Jesse, B. J. Rodriguez, and S. V. Kalinin, e-print arXiv:cond-mat/0610764.

[84] S. V. Kalinin, E. A. Eliseev, and A. N. Morozovska, Appl. Phys. Lett. **88**, 232904 (2006).

[85] E. A. Eliseev, S. V. Kalinin, S. Jesse, S. L. Bravina, and A. N. Morozovska, J. Appl. Phys. **102**, 014109 (2007).

[86] A. N. Morozovska, E. A. Eliseev, S. L. Bravina, and S. V. Kalinin, Phys. Rev. B **75**, 174109 (2007).

[87] J. X. Zhang, Y. L. Li, Y. Wang, Z. K. Liu, L. Q. Chen, Y. H. Chu, F. Zavaliche, and R. Ramesh, J. Appl. Phys. **101**, 114105 (2007).

[88] S. V. Kalinin, S. Jesse, B. J. Rodriguez, E. A. Eliseev, V. Gopalan, and A. N. Morozovska, Appl. Phys. Lett. **90**, 212905 (2007).

[89] T. Zhao and R. Ramesh, personal communication (2006).

[90] P. E. Sheehan and L. J. Whitman, Phys. Rev. Lett. **88**, 156104 (2002).